Support information

Magnetic Field Control in Growth Process of Co_3O_4 and Its Performance Enhancement Mechanism as Anode Material for Lithium Ion Capacitors

Fusen Lv, Rui Chen, Xiao Yang, Jiaqi Liu, Tie Liu, Kai Wang, Xiaoming Liu, Hao Li, Leiming Fang, Qiang Wang, Shuang Yuan

Methods

Assembly of LIB and LIC. Co_3O_4-M (Co_3O_4) was mixed with acetylene black, polyvinylidene fluoride (PVDF) and N-methyl-2-pyrrolopyrone (NMP) at a ratio of 7:2:1 to form a slurry, which was evenly coated on the surface of the copper foil sheet to obtain a negative electrode piece, and the lithium sheet was used as the pair electrode, and the ethylene carbonate (EC) and dimethyl carbonate (DMC) solution of 1 mol/L lithium hexafluorophosphate (where the mass ratio of EC to DMC was 15:45) was used as the electrolyte, and the lithium-ion battery was assembled in a glove box. The assembly steps of the LIC are similar to those of the LIB, except that the lithium piece is replaced with a positive electrode piece. (Activated carbon, acetylene black, polyvinylidene fluoride (PVDF) and N-methyl-2-pyrrolopyrone (NMP) were mixed in a ratio of 7:2:1 to form a slurry, which was evenly coated on the surface of the aluminum foil sheet to obtain the positive electrode piece).

Material characterization. The microstructures of the as-prepared materials were characterized by scanning electron microscopy (SEM, ZSISS GeminiSEM 300) at 3 kV, transmission electron microscopy (TEM, FEI Talos F200X G2) at 200 kV, and aberration-corrected HADDF-STEM (FEI Themis Z) at 200 kV. X-ray diffraction (XRD) patterns were conducted with a Rigaku Ultima IV diffractometer. Fourier

transform infrared (FT-IR) spectrum was performed on a Bruker ALPHA spectrometer using KBr pellets. Ultraviolet-visible absorption spectra (VIS) was performed on a PE lambda 750. X-ray photoelectron spectroscopy (XPS) was conducted using a Thermo Scientific K-Alpha instrument with Al Kα radiation to analyze the chemical composition. Thermogravimetric analysis (TG) was performed on a Rigaku TGA 550 between 30℃ and 800℃ at a heating rate of 10 ℃/min in the Ar atmosphere. Horiba LabRAM HR Evolution confocal microscopy Raman spectrometer. The specific surface area was calculated by analyzing the N2 adsorption/desorption isotherms (Quantachrome Nova 4000e) of Brunauer-Emmett-Teller (BET). Electron paramagnetic resonance (EPR) measurements were conducted with Bruker EMXplus-6/1. The zero-field cooling (ZFC) temperature-dependent magnetic susceptibility was measured by superconducting quantum interference devices (Quantum Design PPMS-9) with a temperature range from 3 to 300 K under the magnetic field of 1000 Oe. The Co L-edge and O K-edge sXAS spectra were collected at the Soft X-ray magnetic circle dichroic line station of National Synchrotron Radiation Laboratory (NSRL). The O K-edge SRPES spectra were collected at the BL11U beamline of National Synchrotron Radiation Laboratory (NSRL). The cyclic voltammogram (CV) and electrochemical impedance spectroscopy (EIS) were carried out with an electrochemical workstation (VSP, Bio-Logic). The rest of the electrochemical properties tests of Lithium-ion batterie (LIB) and lithium-ion capacitor (LIC) were conducted on a Land battery measurement system (Land, China) under ambient air.

DFT calculations. All the density functional theory (DFT) calculations were performed using the Vienna Ab-initio Simulation Package (VASP). The Perdew-Burke-Ernzerhhof (PBE) form of the generalized gradient approximation (GGA) was employed for the exchange-correlation functional. The interactions between ions and valence electrons were described by the projector augmented wave (PAW) potential. For addressing the strong onsite columbic interaction of Co atoms, the GGA+U approach developed by Dudarev was adopted, and the Hubbard correlation parameter was set as 3.32 eV for Co atoms. Van der Waals (vdW) dispersion corrections are included by using DFT-D3 approach. Integrations in the Brillouin-zone were implemented using the 1×3×3 Monkhorst-Pack special k-point meshes for bulk calculations. A cutoff energy of 520 eV was adopted for the plane-wave expansion of wave functions. For all structural relaxations, the total energy was converged to 1.0×10^{-6} eV, and the force on each atom was smaller than 0.01 eV/Å.

Supplementary Figures and Tables

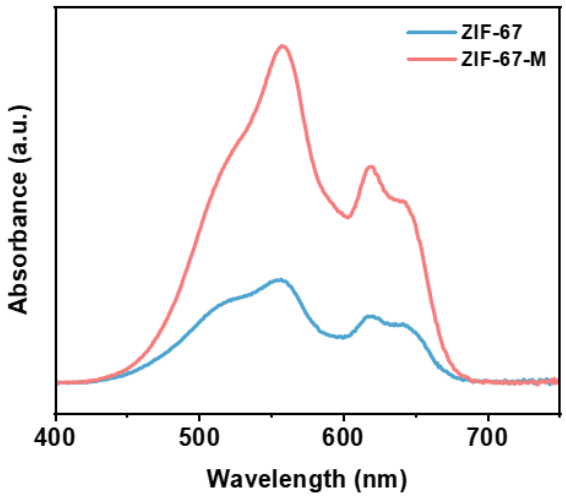

Figure S1. VIS absorption spectrum of the sample after a reaction time of 2 min.

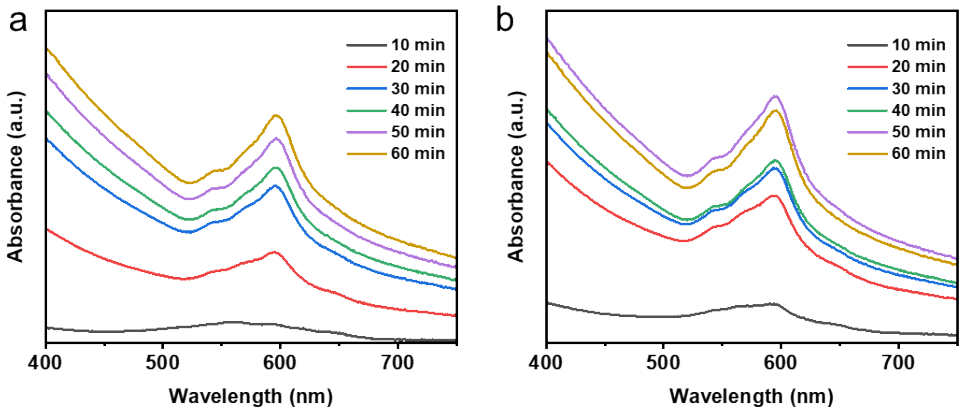

Figure S2. VIS absorption spectrum of the sample. (a) ZIF-67; (b) ZIF-67-M.

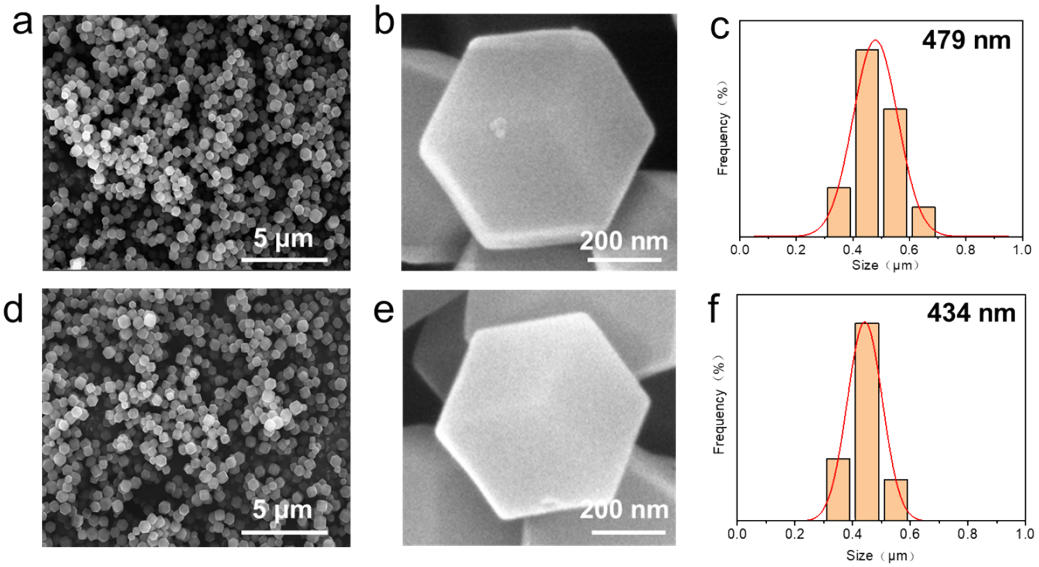

Figure S3. SEM images and particle size statistical of the sample. (a-c) ZIF-67; (d-f) ZIF-67-M.

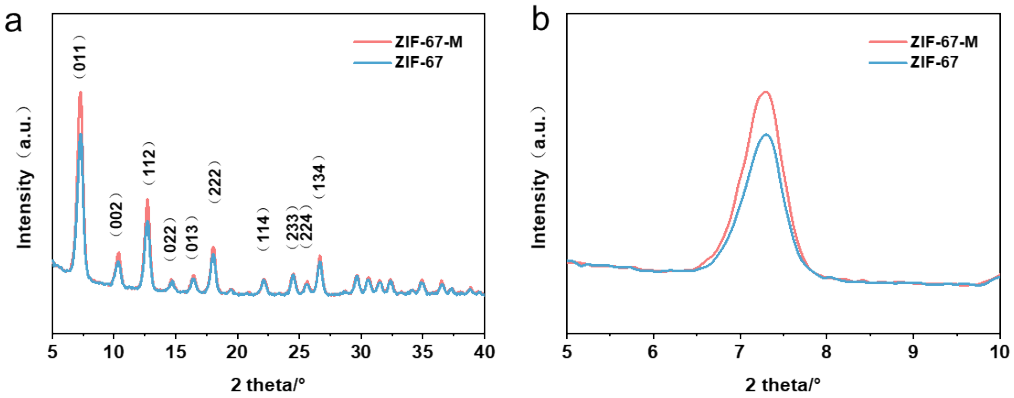

Figure S4. The XRD diffraction pattern of the sample.

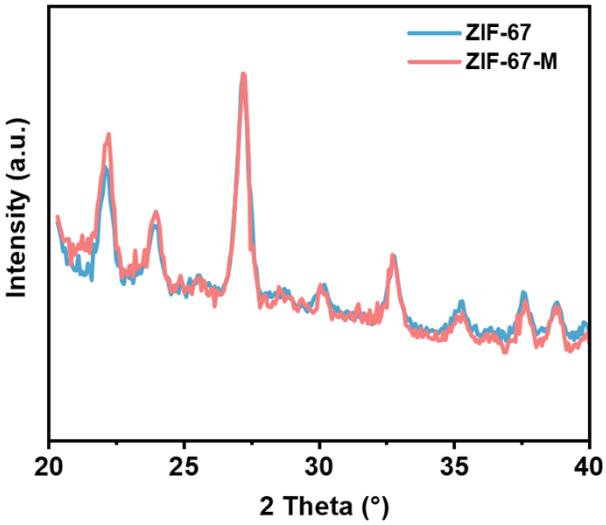

Figure S5. The Neutron diffraction pattern of the sample.

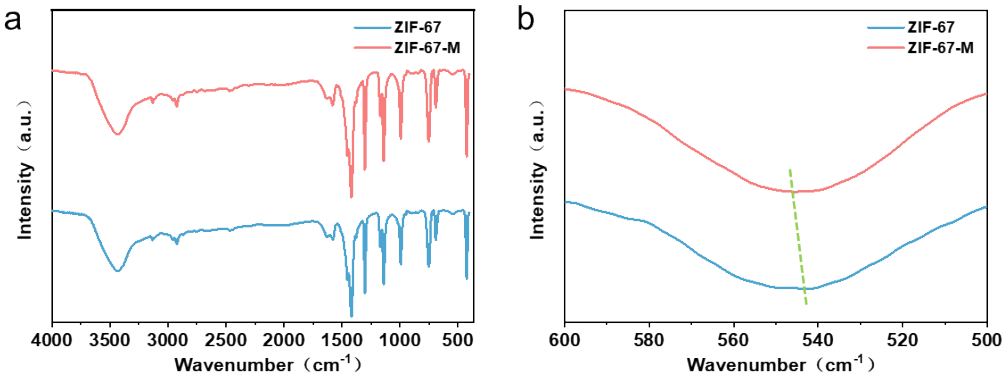

Figure S6. The FT-IR spectra of the sample.

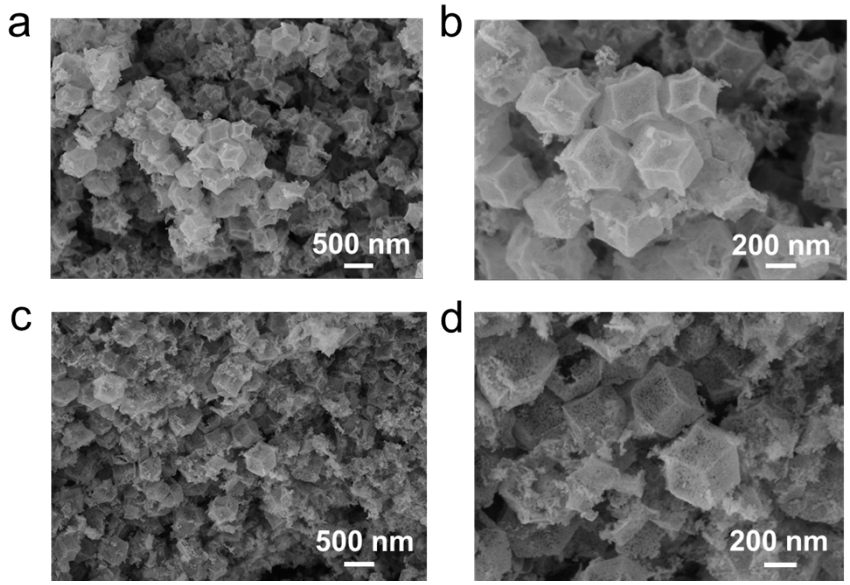

Figure S7. SEM images of the sample. (a-b) Co_3O_4; (c-d) Co_3O_4-M.

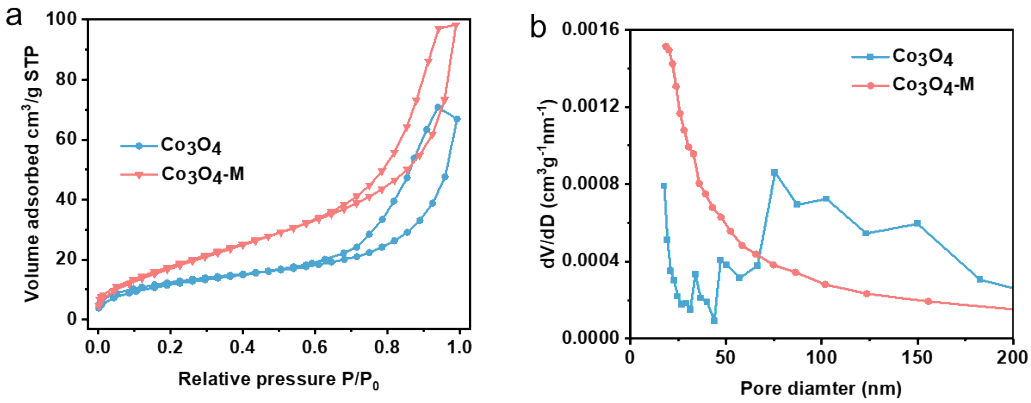

Figure S8. BET analysis and pore size analysis of the sample.

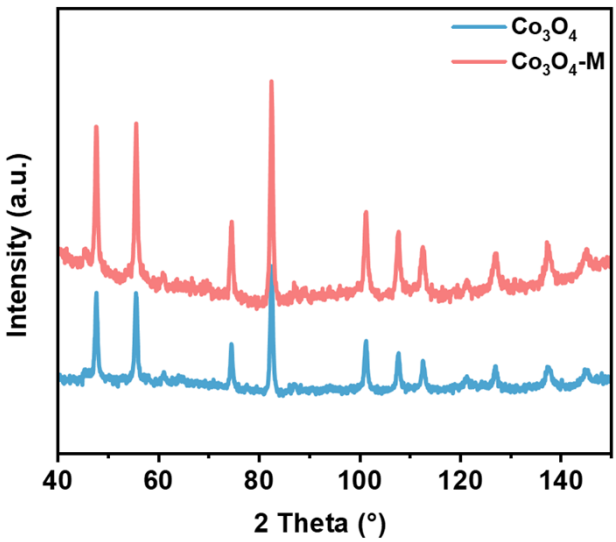

Figure S9. The Neutron diffraction pattern of the sample.

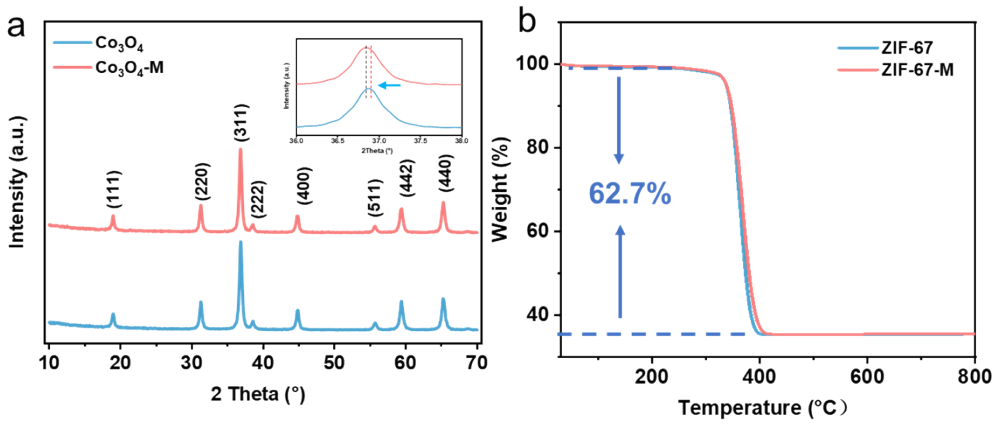

Figure S10. (a) The XRD diffraction pattern of the sample; (b) The TG pattern of the sample.

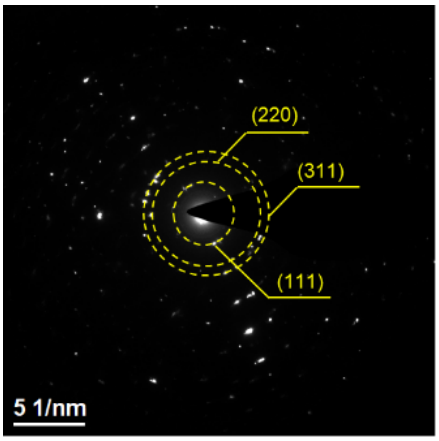

Figure S11. The high-resolution diffraction ring of Co_3O_4

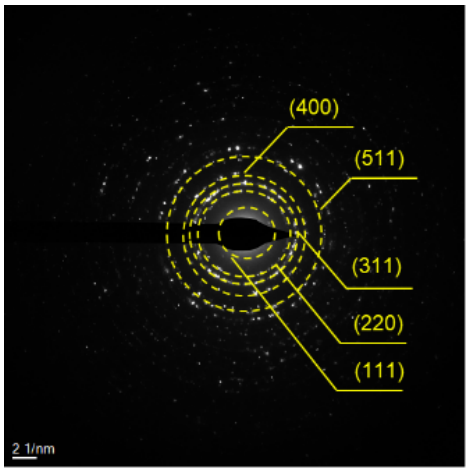

Figure S12. The high-resolution diffraction ring of Co_3O_4-M.

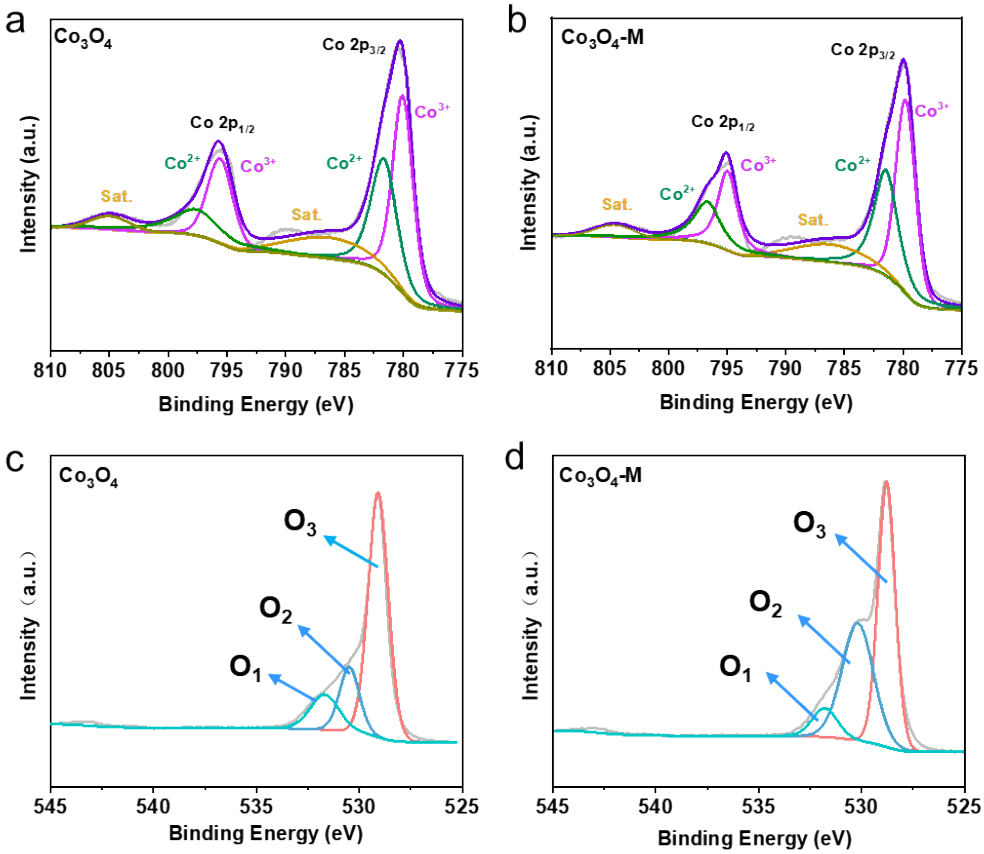

Figure S13. XPS spectra of the sample: (a) (b) Co 2p; (c) (d) O 1s.

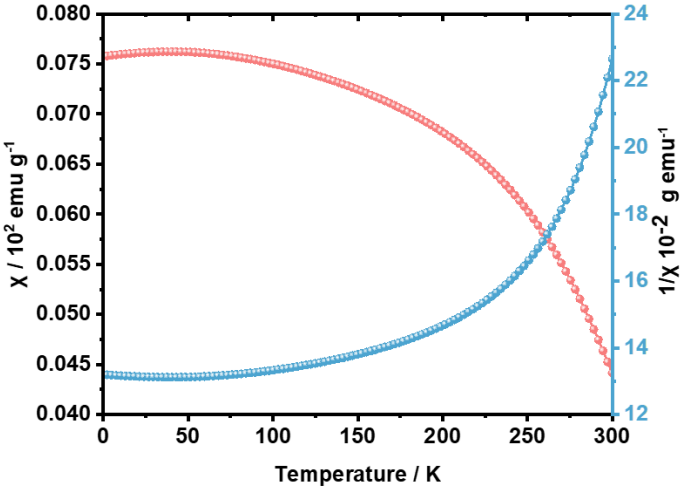

Figure S14. ZFC spectra of the Co_3O_4

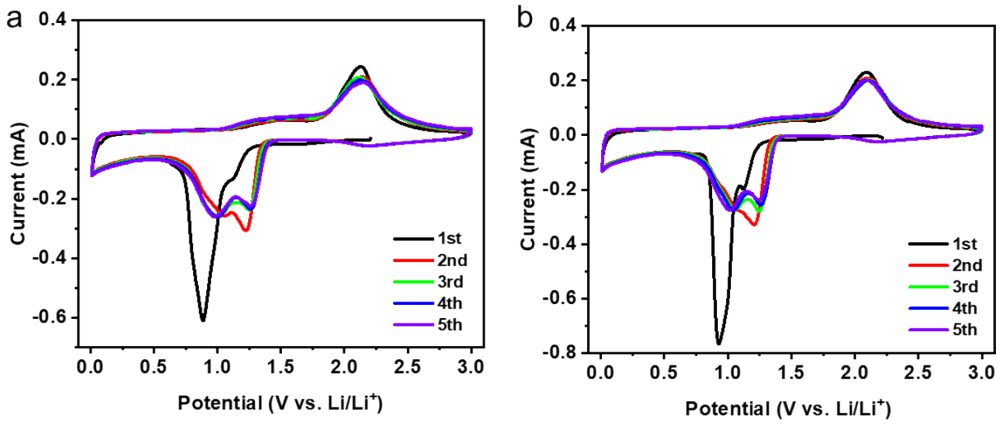

Figure S15. CV cures of the sample. (a) Co_3O_4; (b) Co_3O_4-M.

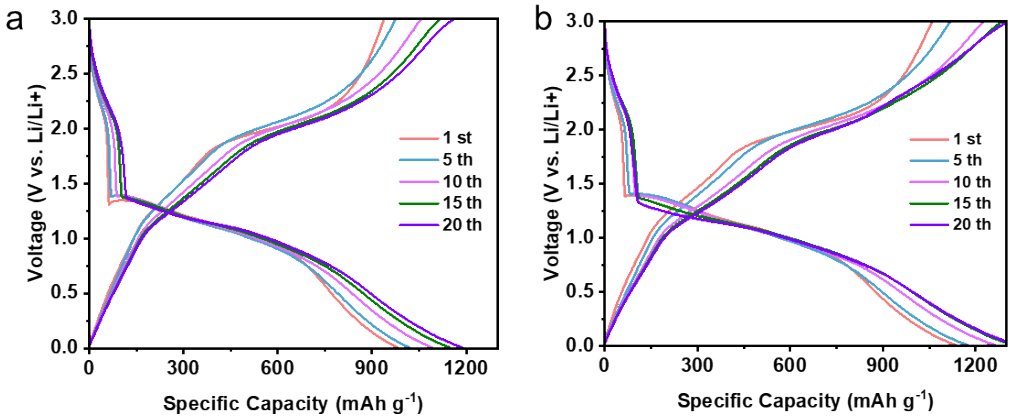

Figure S16. Charge-discharge profiles at a current density of 0.2 A g^{-1}. (a) Co_3O_4; (b) Co_3O_4-M.

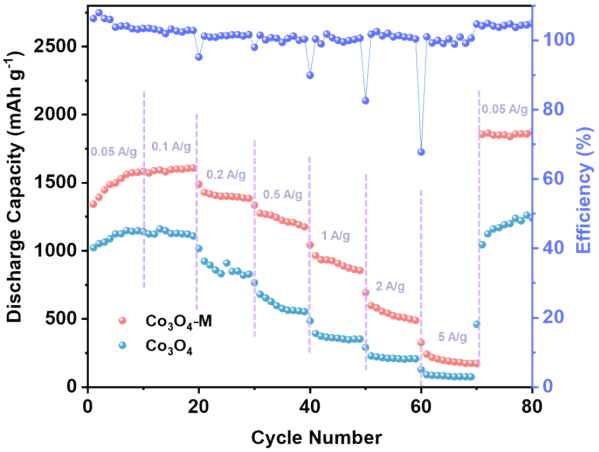

Figure S17. Rate capabilities.

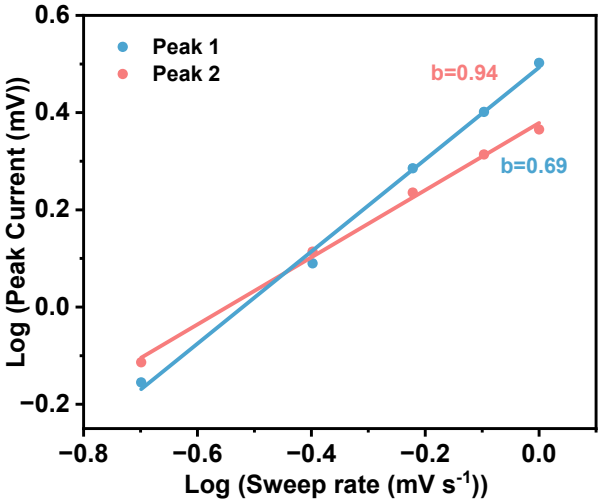

Figure S18. Analysis of *b*-value of the Co_3O_4-M

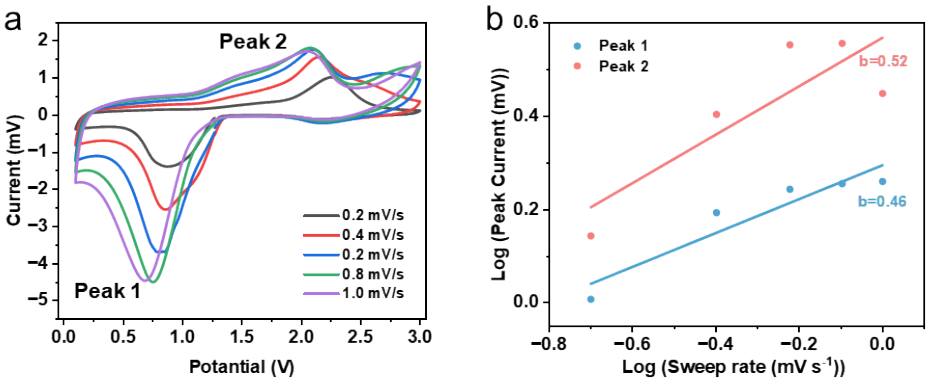

Figure S19. (a) CV curves at various sweep rates of the Co_3O_4.
(b) Analysis of *b*-value of the Co_3O_4

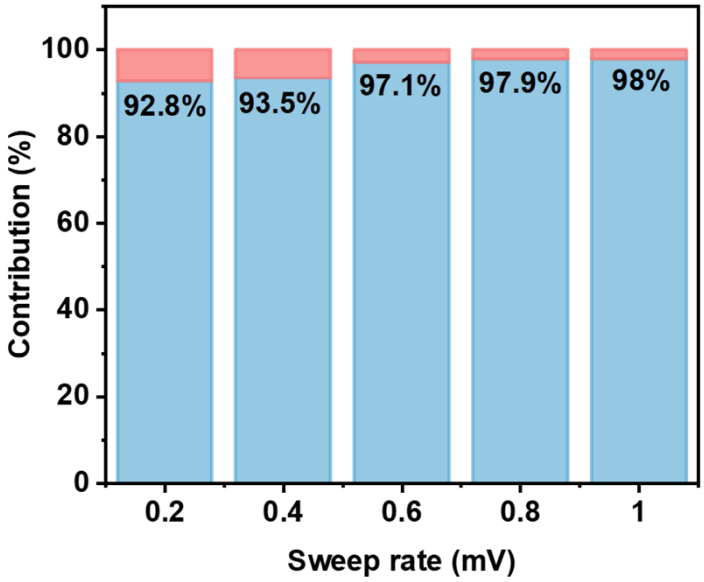

Figure S20. Ratio of pseudocapacitive contributions at different scan rates for Co_3O_{4-x}.

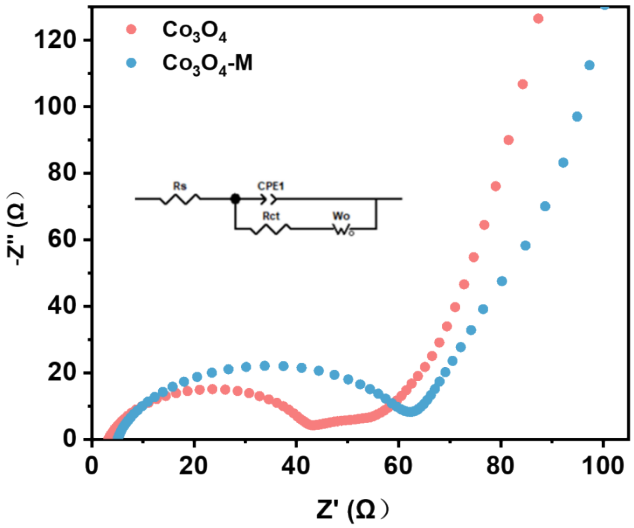

Figure S21. EIS of the Co_3O_4–M and Co_3O_4 electrodes

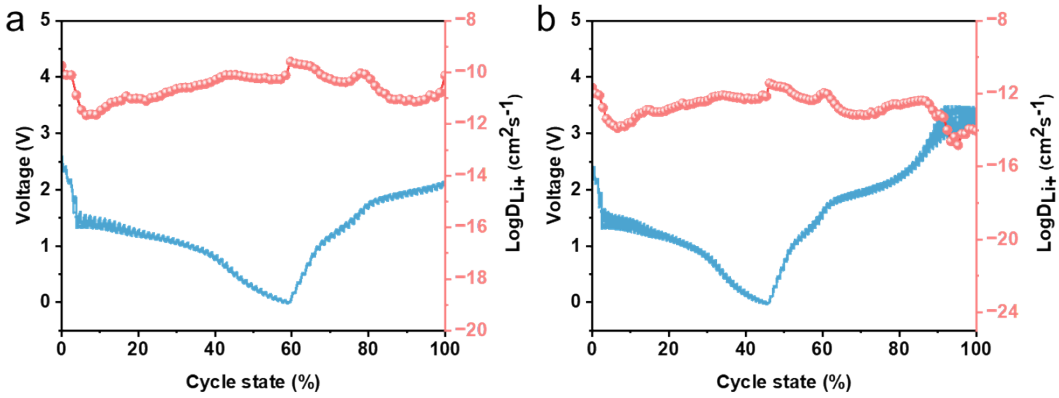

Figure S22. GITT of the Co_3O_4−M and Co_3O_4 electrodes

Table S1 Comparison of the performance of the Co_3O_4-M with that of other reported LIBs.

Sample	Current density（mA/g）	Cycle number	Capacity (mAh/g)	Ref.
Co_3O_4/N-C	100	100	423	48
$5Co_3O_4/CeO_2$	100	100	1131.2	49
Co_3O_4@CuO@GQDs	100	200	1054	50
Co_3O_4/MXene	1000	1000	620.4	51
Co_3O_4/C	500	400	773	52
Co_3O_4/N-CNTs-CNF	178	100	999	53
NiO/Co_3O_4	100	100	1428.8	54
H-Co_3O_4@CNT	1000	150	752	55
H-N-C@Co_3O_4/CNT	200	130	1468	56
Co_3O_4/N-C	200	300	1510	This work

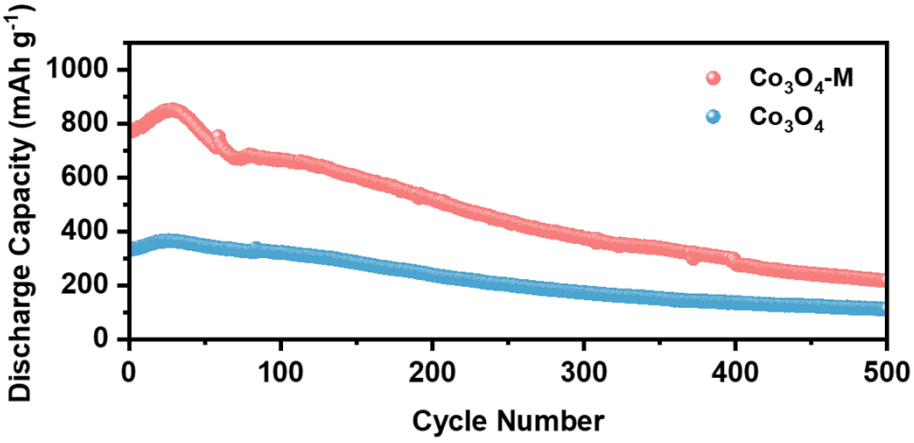

Figure S23. Cycling performance at a current density of 1 A g^{-1}

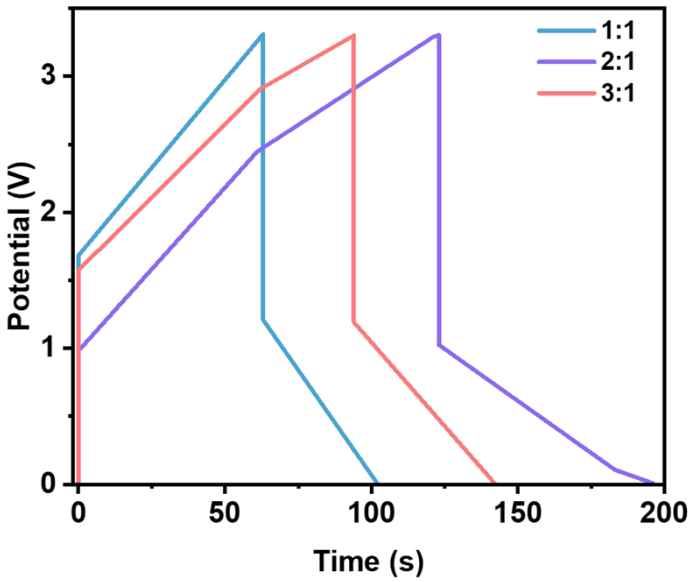

Figure S24. Voltage-time graph of different proportions of Co_3O_4-M at a current density of 1 A g^{-1}

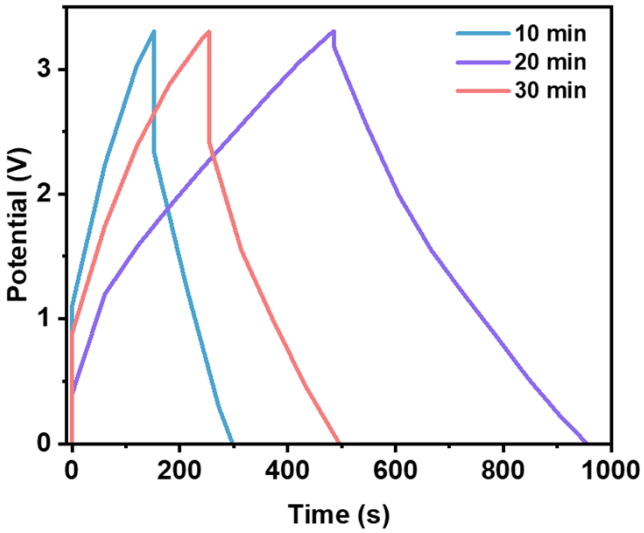

Figure S25. Voltage-time graph of different pre-physicochemical times of Co_3O_4-M at a current density of 1 A g^{-1}

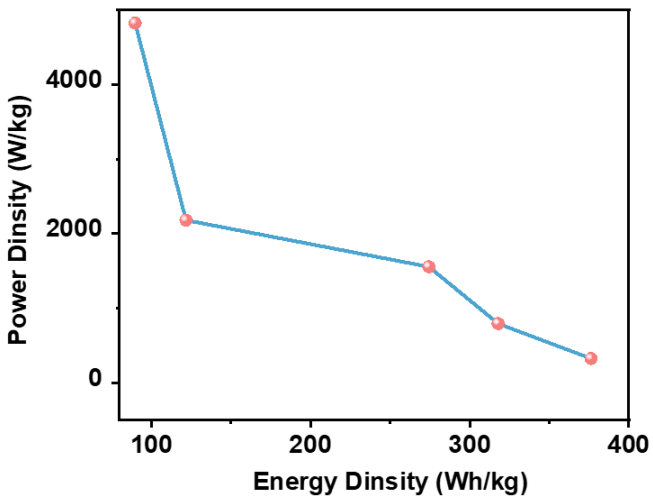

Figure S26. Energy density and power density range of Co_3O_4-M

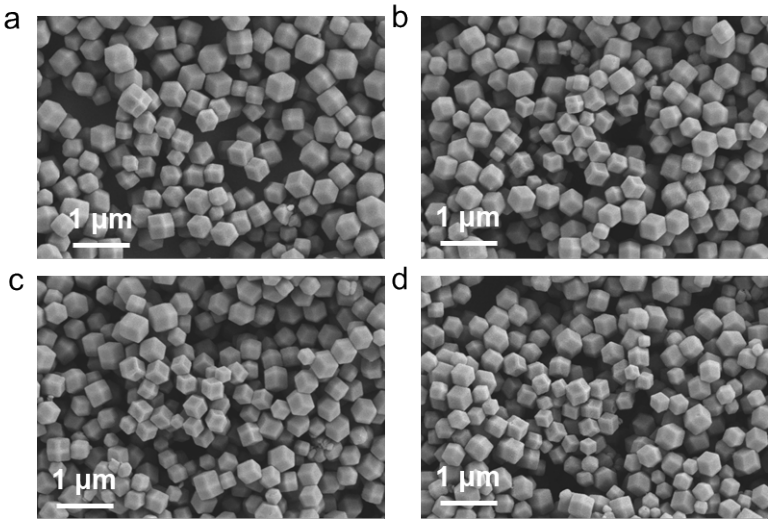

Figure S27. SEM images of the sample. (a) ZIF-67-1:10; (b) ZIF-67-1:12; (c) ZIF-67-1:14; (d) ZIF-67-1:16

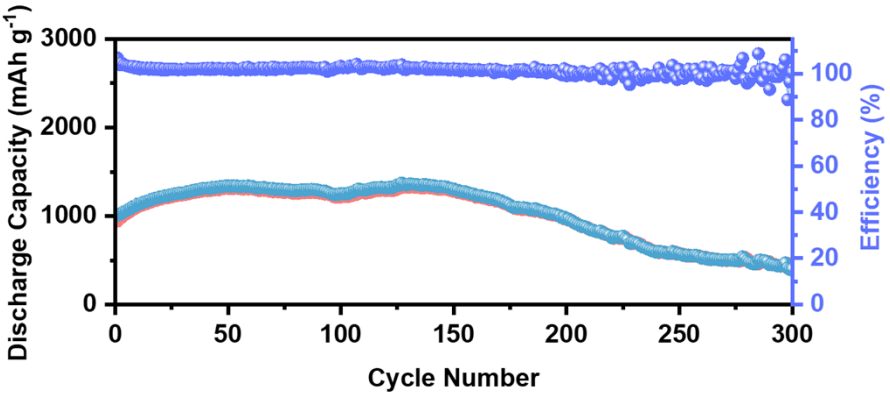

Figure S28. Cycling performance of Co_3O_4-1:16 at a current density of 0.2 A g^{-1}

Table S2 Comparison of the cycling performance of different anodes

Anode	1st	150th	200th	300th
Co_3O_4-M	1134 mAh g^{-1}	1391 mAh g^{-1}	1633 mAh g^{-1}	1510 mAh g^{-1}
Co_3O_4	981 mAh g^{-1}	1034 mAh g^{-1}	1227 mAh g^{-1}	694 mAh g^{-1}
Co_3O_4-1:16	1008 mAh g^{-1}	1305 mAh g^{-1}	965 mAh g^{-1}	396 mAh g^{-1}